
SHORT-TERM SOLAR IRRADIANCE FORECASTING UNDER DATA TRANSMISSION CONSTRAINTS

A PREPRINT

Joshua E. Hammond^{*1}, **Ricardo A. Lara Orozco**^{†2}, **Michael Baldea**^{‡1,3}, and **Brian A. Korgel**^{§1,4}

¹McKetta Department of Chemical Engineering, The University of Texas at Austin, Austin, TX 78712

²Hildebrand Austin Department of Petroleum and Geosystems Engineering, The University of Texas at Austin, Austin, TX 78712

⁴Energy Institute, The University of Texas at Austin, Austin, TX 78712

³Institute for Computational Engineering and Sciences, The University of Texas at Austin, Austin, TX 78712

March 19, 2024

ABSTRACT

We report a data-parsimonious machine learning model for short-term forecasting of solar irradiance. The model inputs include sky camera images that are reduced to scalar features to meet data transmission constraints. The output irradiance values are transformed to focus on unknown short-term dynamics. Inspired by control theory, a noise input is used to reflect unmeasured variables and is shown to improve model predictions, often considerably. Five years of data from the NREL Solar Radiation Research Laboratory were used to create three rolling train-validate sets and determine the best representations for time, the optimal span of input measurements, and the most impactful model input data (features). For the chosen test data, the model achieves a mean absolute error of $74.34 W/m^2$ compared to a baseline $134.35 W/m^2$ using the persistence of cloudiness model.

1 Introduction

The United States has set an aggressive target to achieve a power grid with net-zero greenhouse gas emissions by 2035 [1, 2, 3]. This will require a major shift in the power generation mix from fossil fuels, to include significantly more renewable sources, such wind and solar [3, 4, 5]. Since wind and solar power generation are intermittent and largely non-dispatchable, it will become increasingly important to anticipate fluctuations in renewable power generation to ensure the stability of the grid. Accurate near-term forecasts of solar photovoltaic (PV) power generation will be especially important to ensure that power supply meets demand.

The economic impact of PV forecasts is considerable[6]. Accurate near-term forecasts enhance grid stability by anticipating the need for ramping events[7, 8, 9, 10], and could be used to define targets for demand response and help firm generation[11, 12], advise real-time market price predictions[13], and inform ancillary service dispatch[14, 15].

Short-term forecasts of PV generation rely on large volumes of diverse, high-dimensional data including local meteorological measurements, numerical weather prediction[16], and satellite images[17]. Sky cameras are becoming an increasingly widespread method for gathering local information at generation sites [18, 19, 20]. Because of the computational power needed to make PV generation forecasts, local measurements are usually processed at a centralized facility or data center[16]. Solar PV facilities are typically placed in remote locations, and transmitting the required data (particularly, sky camera images) from the generation sites to centralized computing facilities can be difficult due to data infrastructure limitations and costs.

*joshua.hammond@utexas.edu

†rlara@che.utexas.edu

‡mbaldea@che.utexas.edu

§korgel@che.utexas.edu

It is precisely this problem that we address in this work. We introduce a machine learning model to forecast solar irradiance over the near term, that is data parsimonious and minimizes data transmission requirements. The model uses a set meteorological station data and *scalar* data extracted from sky camera images as inputs. Feature importance studies are used to discern the most impactful features in the available set. Inspired by control theory, a noise signal (along with the corresponding noise model) is introduced to capture unmeasured disturbances. The residual (difference) between the persistence of cloudiness (POC) prediction and true irradiance over the forecast horizon is utilized as the output. While the final model is less accurate than recently published sky camera-based forecasting models, it requires orders of magnitude less data transmission, and significantly outperforms reference forecasts.

The specific contributions of this work are:

- A parsimonious machine learning model for near-term forecast of solar irradiance using scalar features. This model is designed to minimize data transmission requirements from remote generation sites and requires significantly less bandwidth than existing models.
- A novel approach to forecasting solar irradiance by predicting the deviation from the persistence of cloudiness model. This approach is predicated on eliminating the need to capture known long-term dynamics, and is shown to improve forecast accuracy (compared to including persistence information as a model input).
- A noise model is used – to our knowledge, for the first time in this application area – to account for unmeasured variables/disturbances, and is shown to further improve forecasting accuracy.
- New empirical insights on feature importance and the effect of input sequence length on model performance are drawn from a large-scale data set.

Nomenclature

General Abbreviations

ASI	All Sky Imager
BMS	Baseline Measurement System
CNN	Convolutional Neural Network
FSS	Forecast Skill Score
LSTM	Long Short-Term Memory
MAE	Mean Absolute Error
nMAP	Normalized Mean Absolute Percentage Error
NREL	National Renewable Energy Laboratory
NWP	Numerical Weather Prediction
POC	Persistence of Cloudiness
PV	Photovoltaic
RMSE	Root Mean Square Error
SRRL	Solar Radiation Research Laboratory

Time Representations

\angle	Sine and Cosine Transformation
----------	--------------------------------

TM	Time Milestones
ToD	Time of Day
ToY	Time of Year

Irradiance Representations

ΔCSI	Change in Clear Sky Index
ΔGHI	Change in Irradiance
\hat{y}_i	A predicted value
y_i	A true value
CS Dev.	Clear Sky Deviation
CSI_t	Clear Sky Index at time t
DHI	Diffuse Horizontal Irradiance
DNI	Direct Normal Irradiance
GHI	Global Horizontal Irradiance
GHI_0	Irradiance at time of forecast
GHI_t	Irradiance at time t
$GHI_{CS,t}$	Ideal Clear Sky Irradiance at time t

2 Background

The term “solar forecasting” describes the prediction of PV power generation, as well as the prediction of irradiance, given that PV generation is a function of global horizontal irradiance (GHI, W/m^2) and panel temperature [21]. While cloud cover and position have the largest impact on irradiance [22, 23, 24] –sometimes accounting for a change in irradiance of over 80% in a minute– other variables such as dispersed particles and wind[25] are linked to irradiance as well. As shown in Equation (1), GHI is composed of both direct and diffuse sunlight, where DNI is the direct normal irradiance, α is the solar zenith angle, and DHI is the diffuse horizontal irradiance. Clear sky models calculate GHI in the absence of atmospheric effects using time and global position[21, 26, 27, 28]. The ratio of measured irradiance (GHI_t) to ideal clear sky irradiance ($GHI_{CS,t}$) at a given time instant t is often referred to as clear sky index (CSI) and is shown in Equation (2).

$$GHI = \cos(\alpha)DNI + DHI \quad (1)$$

$$CSI_t = \frac{GHI_t}{GHI_{CS,t}} \quad (2)$$

Persistence models are often used to evaluate the effectiveness of forecasting algorithms. The persistence of cloudiness (POC) model assumes that the clear sky index at the time of forecast will remain constant throughout the forecast horizon. Equation 3 shows an example POC forecast at 10-minute intervals up to a maximum forecast horizon of 120 minutes.

$$CSI_t = CSI_0, t \in \{10, 20, \dots, 110, 120\} \quad (3)$$

The POC forecast does not take into account fluctuations in weather conditions, but does provide a baseline for near-term solar output forecasting. More sophisticated forecast models should achieve (significantly) higher accuracy compared to the POC model by anticipating changes in weather conditions.

It is common for these latter models to predict the *difference* between the time-varying irradiance and the baseline. This has the effect of de-trending the data [29, 30]. For example, [31, 32] use autoregressive models to predict irradiance relative to a clear sky model (rather than using the POC as a baseline). We note that other de-trending methods, such as wavelet decomposition [33] and spectral decomposition [34] have been recently proposed for irradiance forecasting.

The aforementioned works are restricted to using *scalar* data as model inputs, and the number of inputs is typically small in practical settings.

There is nevertheless a wealth of data that can be relevant to irradiance forecasting. These include local meteorological measurements (cloud height, wind speed and direction, temperature, humidity, and air pressure), sky camera images, Numerical Weather Prediction (NWP) results, and satellite imaging. Some of these data are in non-scalar formats (e.g., camera images) and thus do not lend themselves naturally to use in time-series models.

This fact has motivated the use of machine learning (ML) approaches for irradiance forecasting. Convolutional Neural Networks (CNNs) and Long Short-Term Memory (LSTM) networks are common deep learning architectures used to extract patterns from data and predict sequences, respectively [35].

ML models broadly fall into two categories:

- End-to-end models utilize available data as inputs with little or no pre-processing or interpretation. For example, [36] reported the use of multiple sky cameras to track cloud positions in the sky, and a stereoscopic arrangement was reported by [37] for estimating cloud height. [38] determined current irradiance directly from sky camera images, while [39] used deep learning models to forecast irradiance from similar data.

Some end-to-end models are used for multiple predictions, e.g., both cloud patterns [40, 41, 42] and irradiance [19, 43, 44]. [45] use a deep learning model to determine cloud movement vectors from image sequences as well as forecast irradiance.

These models typically use heterogeneous data formats as inputs. It is worth recalling here the work of [46], who performed feature fusion by leveraging unused image pixels to embed other sensor data before feeding sky-camera images to a deep CNN model.

- Physically-motivated models take a physics-based lens to the data, generating additional insights prior to building the irradiance forecasting model itself. These include detection of cloud position, cloud motion, and identifying position of the Sun, which can be approached via color analysis [47, 48], pixel clustering [49, 50], and convolution methods [51]. Recent work by [17] demonstrated that polar transformations centered on the sun can extract cloud movement toward the sun. [52] use features extracted from a sky camera such as cloud coverage, height, and type as well as parametric relationships such as solar position to predict future irradiance.

We emphasize here that these are *broad* categories and modeling can take inspiration from both. An example is the work of [20], where physics-based fluid-flow equations to predict future irradiance using sky camera images as inputs in an end-to-end structure.

It is also of note that the works referenced here use sophisticated, computationally-intensive and data-intensive architectures to perform the irradiance forecasting task. Local data collected from – typically remote – solar PV generation sites are transmitted over some communication channel to a centralized location for processing and forecasting. This implicitly assumes that there are no data transmission constraints. In practice, however, the communication channel may be (severely) bandwidth limited, and may not be able to accomplish the timely transmission of all the data, particularly sky camera images which are stored in typically large files. This emphasizes the need for developing *data parsimonious* models, that are capable of performing the forecasting task based on a *limited* number of inputs that are readily obtainable over existing bandwidth restricted communication channels.

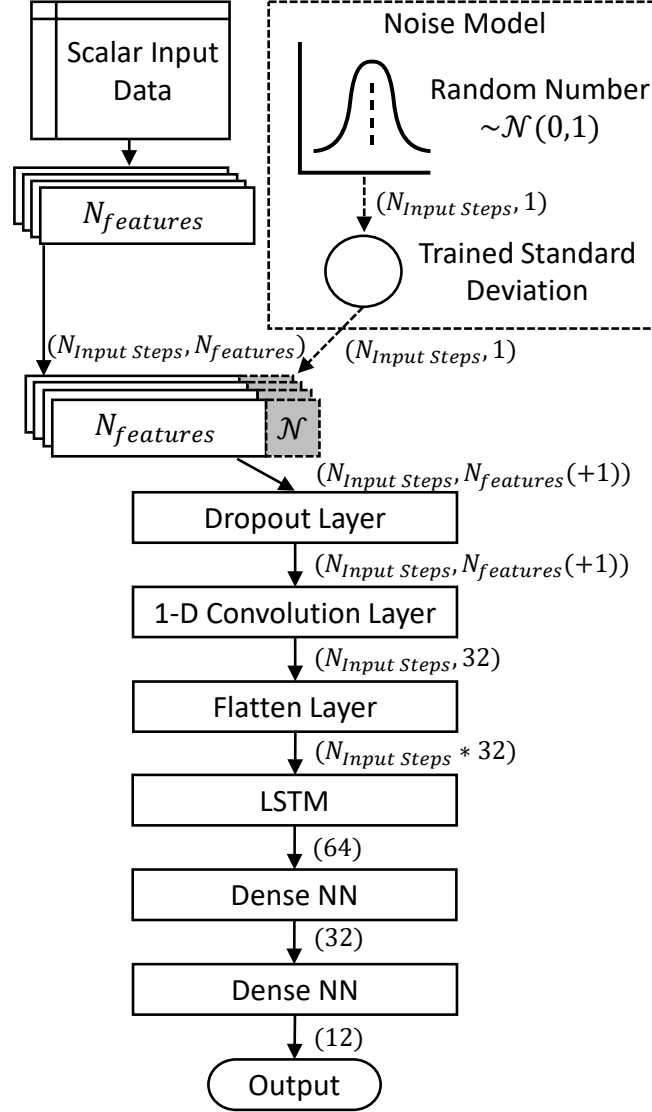


Figure 1: CNN-LSTM Model Structure with an optional noise model where random numbers drawn from a Gaussian distribution to account for unmeasured variables and disturbances. Dimensions are shown in parentheses.

3 Model

Motivated by the above, we present a CNN-LSTM model which uses *scalar* features extracted from a commercially available sky camera to forecast near-term irradiance, expressed as the deviation of actual irradiance from the POC value.

The model uses up to 168 features summarized in Appendix A across five years (2017—2022) from the National Renewable Energy Laboratory (NREL) Solar Radiation Research Laboratory (SRRL) Baseline Measurement System (BMS) [53] in Golden, Colorado, USA. The BMS provides 131 parameters including scalar data extracted from an Eko All Sky Imager (ASI-16) such as light and heavy cloud coverage percentages and whether the sun is covered by clouds [47, 54]. BMS data were augmented with ideal clear sky irradiance data [26, 27, 28, 55] and other engineered features such as lagged statistics. Figure 2 shows an example of measured irradiance values compared to clear sky irradiance values, as well as selected sky images at the time of measurement. A full list of the scalar features extracted from sky camera images as well as a comprehensive list of all features examined in this work is provided in A. We note that the scalar features of the sky camera images are provided by the camera itself and do not require any (additional) local processing or computing power.

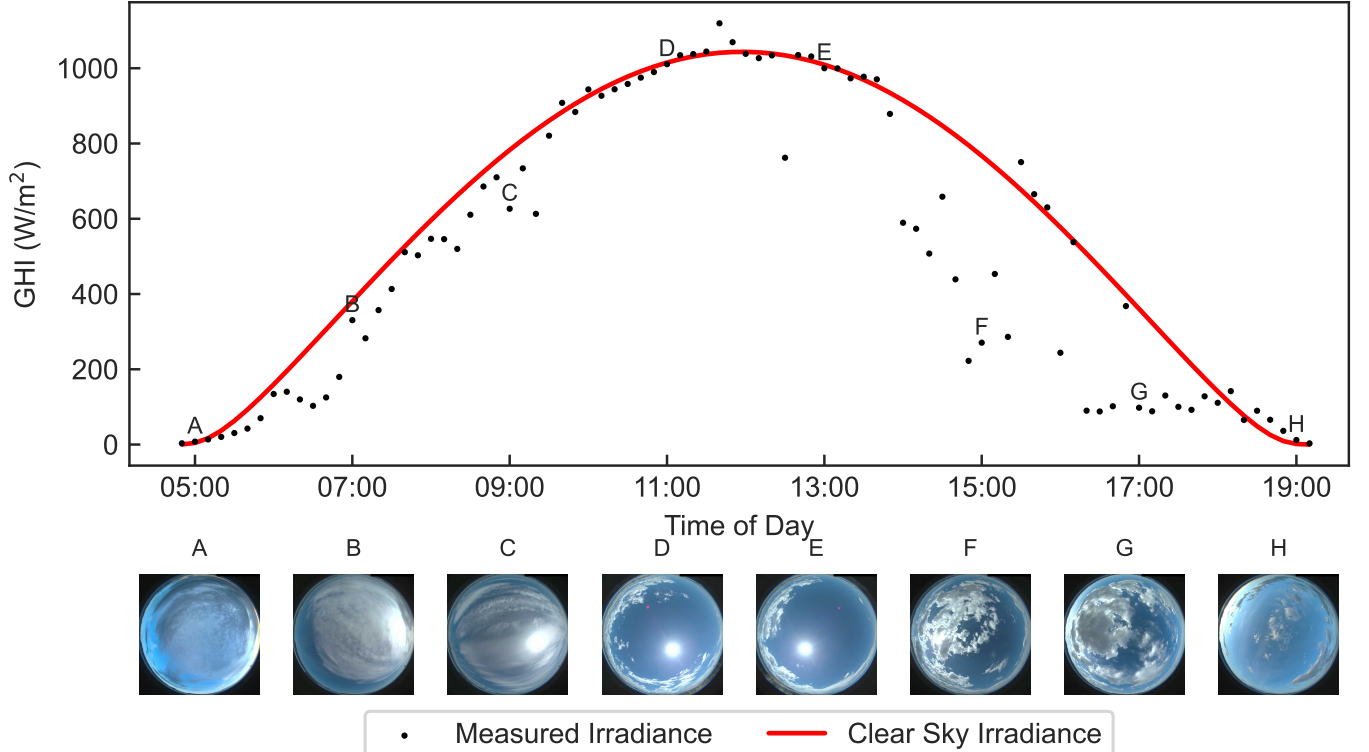


Figure 2: Irradiance measurements and a subset of sky-camera images from May 18, 2022 at the NREL SRRL BMS. Figure created by the authors based on data collected from [53]. Letters denote the moments that the images were collected.

While we focus on predicting irradiance at ten minute intervals up to two hours from the time of forecast, we believe that the model can be easily adapted to other forecast frequencies and prediction horizons.

3.1 Model Architecture and Training

The model architecture is based on using a CNN-LSTM structure as shown in Figure 1. A dropout layer ensures that the model learns sparse and generalizable feature representations and helps prevent overfitting. Next, CNNs efficiently extract intermediate features from input data using convolutional filters learned during model training. The LSTM layer identifies sequential patterns within the training data and is used to identify temporal patterns within the data. The final dense layers perform a bottleneck operation and transform the intermediate representations to the final irradiance sequence prediction over the time horizon considered. We use two dense layers to ensure that the model has sufficient capacity to encode the predicted irradiance.

Similar architectures have been successfully used for irradiance prediction by e.g., [56] and [41]. Nevertheless, our proposed architecture include a novel feature, that, to our knowledge, has not been employed in the field of solar irradiance forecasting. Inspired by forecasting mechanisms used in the literature on model predictive control [57], a noise signal is included as an additional input. This is motivated by the fact that it is natural to expect that the available features/data do not/cannot fully explain or predict the variable of interest (i.e., irradiance). We *hypothesize* that changes in irradiance are also subject to *random, unmeasured* inputs. It is typical to use a Gaussian noise signal with zero mean; additionally we assume that the variance of this signal is unity (which is a deviation from the control literature), and allow for the weight assigned to this signal to change in the training process.

The model was trained using a rolling train-validate data split with three successive steps to refine the initial model. The first step evaluated different representations of time and irradiance. The second step studied the effect of changing the time span of input measurements on validation error. The third step used the results from the previous two steps and implemented permutation feature importance [58] to identify the most impactful features for predictive performance. The training and validation data splits for each step are shown in Table 1.

Table 1: Model training and tuning used three successive steps to refine the initial model with an input block of 131 features and 13 temporal measurements. Count refers to the number of complete input and output data blocks within each date range.

Step	Training Dates	Count	Test Dates	Count	Description
1	Sep. 27, 2017 — Sep. 26, 2019	21,343	Sep. 27, 2019 — Sep. 26, 2020	12,509	Time and Irradiance Representations
2	Sep. 27, 2017 — Sep. 26, 2020	33,852	Sep. 27, 2020 — Sep. 26, 2021	13,256	Input time horizon
3	Sep. 27, 2017 — Sep. 26, 2021	47,108	Sep. 27, 2021 — Sep. 26, 2022	9,199	Feature importance

3.1.1 Step 1 — Time and Irradiance Representations

Time representations include a floating point number between 0 and 1 representing the proportion of time that has passed since the start of a day or year. These are shown as the Time of Day (ToD) and Time of Year (ToY) representations in Equation (4) and Equation (5). Time of day may also be represented relative to key moments in the day such as sunrise, solar noon, and sunset as shown in Equation (6). We refer to a vector containing these three values as Time Milestones (TM). Finally, we include a trigonometric transform of ToD, ToY, and TM as is common for cyclic variables [59]. We denote these representations as \angle ToY, \angle TM, and \angle ToD and their respective equations are shown in Equation (7), Equation (8), and Equation (9).

$$\text{ToD} = (\text{Hours} + \text{Minutes}/60 + \text{Seconds}/3600)/24 \quad (4)$$

$$\text{ToY} = (\text{Day of Year} + \text{ToD})/365 \quad (5)$$

$$\text{TM} = \left\{ \begin{array}{l} \text{ToD}(\text{Time} - \text{Sunrise Time}), \\ \text{ToD}(\text{Time} - \text{Solar Noon Time}), \\ \text{ToD}(\text{Time} - \text{Sunset Time}) \end{array} \right\} \quad (6)$$

$$\angle\text{ToD} = \{\sin(\text{ToD}), \cos(\text{ToD})\} \quad (7)$$

$$\angle\text{ToY} = \{\sin(\text{ToY}), \cos(\text{ToY})\} \quad (8)$$

$$\angle\text{TM} = \{\sin(\text{TM}), \cos(\text{TM})\} \quad (9)$$

Multiple representations of future irradiance were tested as target variables to determine which produced the most accurate forecast. These representations include GHI_t , CSI , CS Dev. (the difference between GHI_t and GHI_{CS} as shown in Equation (10)), as well as two forms that are relative to the conditions at the time of forecast: change in irradiance (ΔGHI), and change in clear sky index (ΔCSI). These relative representations are shown in Equation (11) and Equation (12) respectively. Differencing and auto-regressive approaches similar to these relative representations of irradiance have been shown to improve the predictive ability of statistical models [29, 30].

$$\text{CSDev.} = GHI_{CS} - GHI_t \quad (10)$$

$$\Delta GHI = GHI_t - GHI_0 \quad (11)$$

$$\Delta CSI = CSI_t - CSI_0 \quad (12)$$

3.2 Step 2 — Input Sequence Length

LSTM models use sequential inputs and determine temporal patterns in those inputs to predict future values. During Step 2, we investigate how the number of input measurements affects model performance.

3.2.1 Step 3 — Feature Importance and Noise Model Evaluation

To determine the most important features for the model, we used permutation feature importance [58] which measures the change in model performance when a feature is randomly permuted. To determine the effect of the noise model, we tested model performance across all three training-validation data set splits with and without the noise model.

3.2.2 Evaluation Metrics

During the training process, accuracy is measured in terms of Mean Absolute Error (MAE), shown in Equation (13). Here, y_i represents the true value and \hat{y}_i represents the predicted value. For an equitable comparison, model statistics are calculated in terms of GHI . To compare to other models in the literature we also calculate Root-Mean Square Error (RMSE), normalized Mean Absolute Percentage error (nMAP), as well as Forecast Skill Score (FSS) which measures performance relative to the POC model. These are defined as follows in Equation (14), (15) and (16) respectively:

$$MAE = \frac{1}{N} \sum_{i=1}^N |y_i - \hat{y}_i| \quad (13)$$

$$RMSE = \frac{1}{N} \sum_{i=1}^N \sqrt{(y_i - \hat{y}_i)^2} \quad (14)$$

$$nMAP = \frac{1}{N} \sum_{i=1}^N \frac{|y_i - \hat{y}_i|}{\frac{1}{N} \sum_{i=1}^N y_i} \times 100 \quad (15)$$

$$FSS = 1 - \frac{y}{y_{POC}} \quad (16)$$

4 Results

4.1 Step 1 — Time and Irradiance Representations

Figure 3 shows the validation MAE of all predictions (t+10 min. to t+120 min) of the model trained with different representations of time and future GHI during the first model refining step. The ToD and ToY representation of time and the ΔCSI representation of future irradiance achieve the lowest MAE across all predicted values in Step 1. Other time representations performed similarly, however, ToD and ToY allow the model to capture daily and yearly cyclical patterns without increasing the number of variables and increasing the likelihood of overfitting.

ΔCSI in conjunction with ToD and ToY as time representations achieves the lowest error among the models tested in Step 1. All models trained with target variables that incorporate information from the clear sky model outperform those that use GHI. Incorporating the known patterns of the Sun using the clear sky model allows the model to isolate the unknown interest: the measured irradiance. Both relative measures of irradiance appear to be more tightly distributed around the center, as shown in Figure 4. This likely facilitates easier recognition of patterns which deviate from the present conditions.

Figure 5 shows the FSS of the best model for each future irradiance representation and demonstrates that models trained with relative representations of future irradiance are better able to anticipate changes in irradiance than models trained with other forms of irradiance. Of the two relative irradiance forms, Figure 6 suggests that ΔCSI is likely a better target variable since clear sky index is more strongly autocorrelated (as defined in Equation (17)) at later lags than GHI or CS Dev.

$$r_s = \frac{cov(R(X), R(Y))}{\sigma_{R(X)} \sigma_{R(Y)}} \quad (17)$$

4.2 Step 2 — Input Sequence Length

The results from varying the number of sequential measurements in Step 2 are displayed in Figure 7. Surprisingly, models trained with fewer input data measurements have lower error than models that include more contextual information. However, [19] note that a model performs best with only the two most recent images as input. By providing

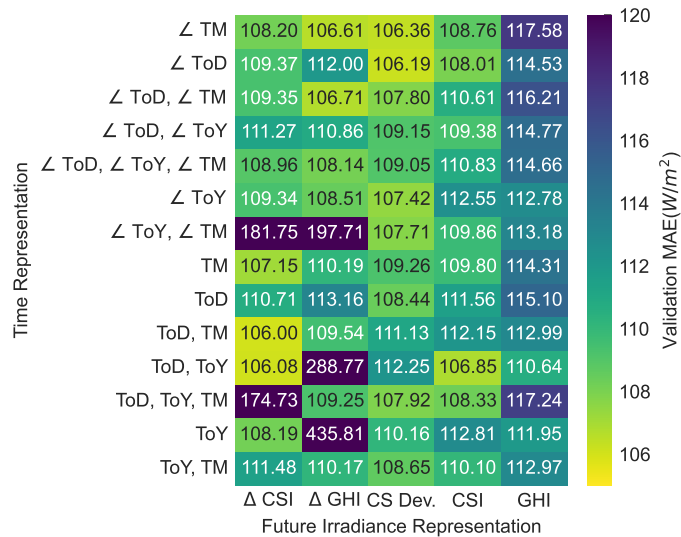


Figure 3: Validation Mean Absolute Error (W/m^2) across all predicted points ($t + 10$ to $t + 120$) for each model trained during Step 1 using year 3 as the test set. In this graphic, each row represents a different combination for time representation and each column represents a method for irradiance representation.

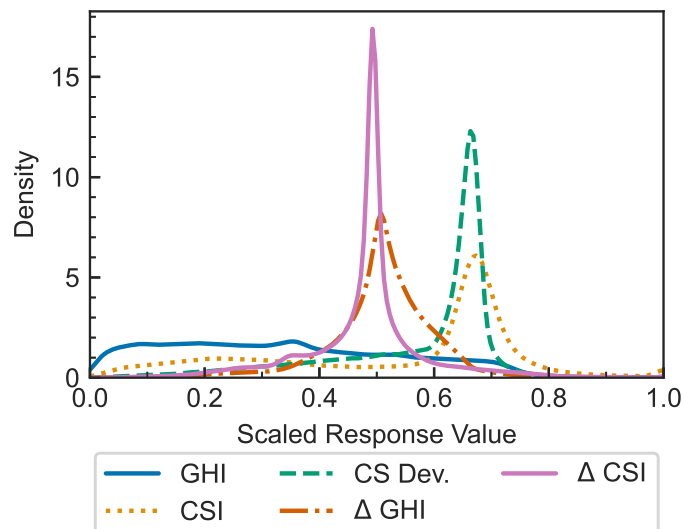


Figure 4: Probability density functions of the future irradiance representations. Note that the relative irradiance representations are much more tightly distributed around the center likely facilitating easier recognition of patterns which deviate from the present conditions.

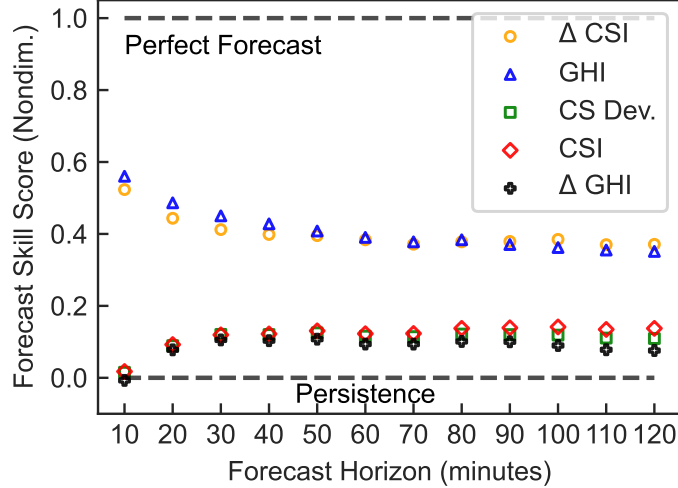


Figure 5: FSS for a model trained on each future irradiance representation.

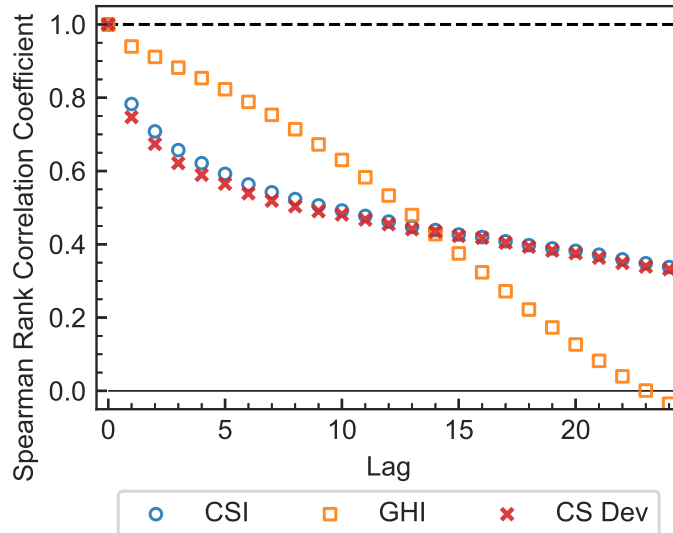


Figure 6: Autocorrelation for three representations of future irradiance beginning 2 hours or 12 lags before a prediction and extending over a two hour prediction horizon.

less input data, the stochastic training process is less likely to result in overfitting. Because of these results, Step 3 focused on modeling an input sequence of one measurement — an input temporal horizon of 0 minutes.

4.3 Step 3 — Feature Importance and Noise Model

Figure 8 shows the results from Step 3, a feature importance test [58], which was used to determine which of the 168 features were most meaningful for the accuracy of GHI predictions. The test systematically corrupts one feature of the input data at a time, and observes the impact on model performance. Large increases in error indicate that a particular feature is valuable to the forecast accuracy while negligible changes in error indicate that the model may not use that feature.

The ten most important features identified in Step 3 are shown in Table 2 with the associated increase in MAE when they are corrupted. Most of the identified features (with exception to the photometers which measure dispersed aerosols) can be obtained with historical measurements, the clear sky model, and a low-cost sky-camera. Notably, two photometer measurements of Aerosols are within the top 10 results. Expensive equipment such as a photometer is not likely to be widely used in practice. When the model is retrained with the 8 remaining inputs, it achieves a MAE of 77.36 W/m^2 , a sacrifice of only 2.16 W/m^2 . This observation could influence equipment selection at sites interested in irradiance forecasting.

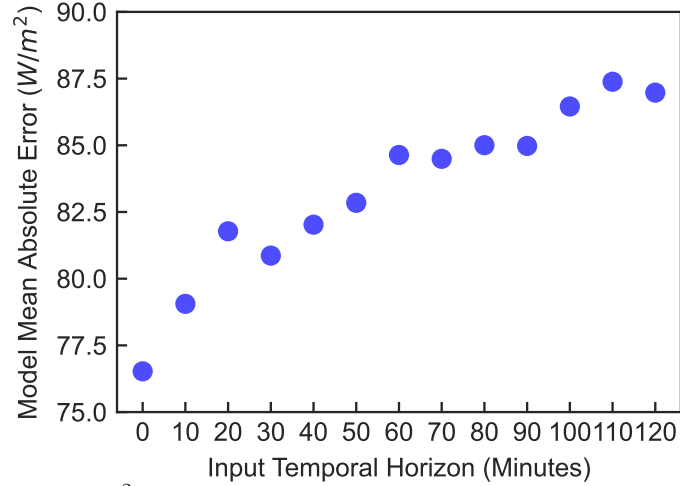


Figure 7: Mean Absolute Error (W/m^2) across all predicted points ($t + 10$ to $t + 120$) of models trained during Step 2 with increasing input time horizons. Each of these models used Δ CSI as the irradiance representation and ToD, ToY as the time representation based on the results in Step 1.

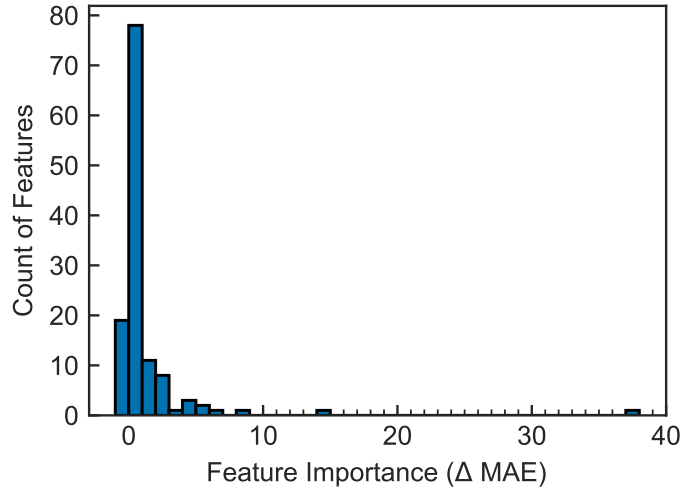


Figure 8: Feature Importance distribution for the features studied

Table 2: Ten most important features of 131 total features as shown by the increase in predicted irradiance MAE as each feature is corrupted. Total cloud cover and GHI clear sky index contribute to prediction accuracy significantly more than other features.

Feature	Feature Importance (MAE)
CDOC Total Cloud Cover	37.76
CSI GHI	14.22
DNI_{t-4}	8.08
940nm Aerosols	6.00
Mean CSI DNI Deviation	5.62
675nm Aerosols	5.20
CSI DNI	4.88
Solar Elevation	4.73
CSI DNI Deviation	4.08
DNI_{t-9}	3.06

Table 3: Validation error across all 3 steps of model refinement. Bold numbers indicate the best (or nearly-best) errors for each step. Results with and without the noise model as well as with all features and the top 10 features are shown. Results indicate that the noise model eliminates the drop in performance when the model is trained with fewer features.

Noise Model	Features	Validation Error (W/m^2)		
		Step 1	Step 2	Step 3
Not Included	All	89.35	76.85	75.20
	Top 10	94.61	83.93	77.36
Included	All	91.07	76.01	74.95
	Top 10	88.96	76.01	74.34

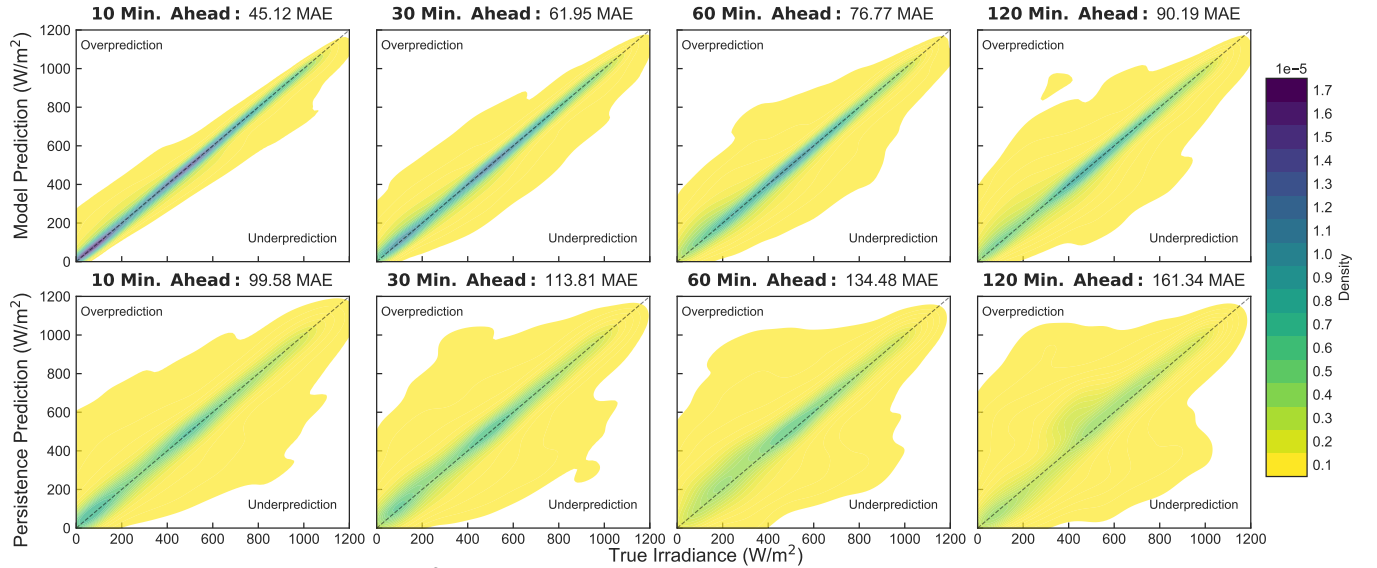


Figure 9: Mean Absolute Error (W/m^2) distribution the model and POC. As expected, the error increases as time from the forecast (the time horizon) also increases. Density near the correct prediction is notably higher compared to the persistence of cloudiness model. MAE across all predicted intervals is $75.20 W/m^2$

The impact of the noise model is also evaluated during this step. Table 3 shows the validation error across all three train-validation data set splits. The architecture including the noise signal performs consistently better than the case without the noise model, and often significantly better. More importantly, using the noise signal input eliminates the drop in performance when the model is trained with fewer features—with a final MAE of $74.34 W/m^2$. This confirms our initial hypothesis that the noise model accounts for both the dropped features and other unmeasured disturbances.

5 Discussion

The final model achieves a MAE of $75.20 W/m^2$, while the POC model has an overall accuracy of $134.35 W/m^2$. The distribution of predictions and true values of the final model is shown in Figure 9 with the persistence model shown below for comparison. These graphs display the normalized density of predicted and true irradiances such that the integrated density on each image is equal to one. The dashed black line shows a perfect forecast; higher concentrations of the plotted prediction values near this line represent better models. The proposed model reduces the gap between true and predicted irradiance compared to the persistence model. However, the distributions become similar as the prediction horizon increases.

Individual predictions are shown for four sample days in Figure 10. Notably, POC and the proposed model perform similarly in environments with low irradiance (top left) or relatively constant environments (top right). On days with large ramping events in irradiance (bottom) the proposed model is better able to anticipate changes in regime, though sometimes these predictions are too aggressive. The results of this work are shown relative to recent literature values collected at the same location in Table 4. It is notable that the models proposed in the literature require sequences of images as inputs (and thus have high data transmission requirements) while the model proposed in this work only uses the features extracted from the images, and is thus data-parsimonious.

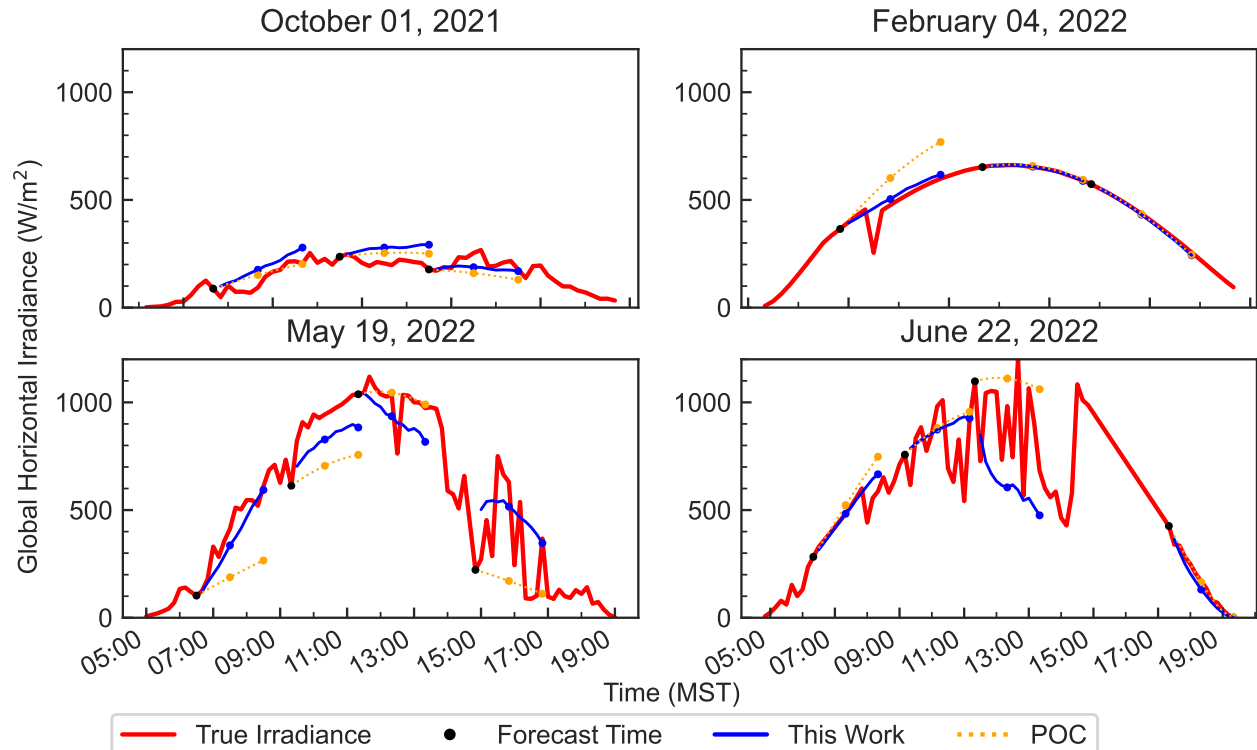


Figure 10: True irradiance as well as the predicted irradiance using the final model and POC across four days in the final validation set.

Table 4: RMSE (W/m^2) of this work, POC, and reported errors from recent literature

Forecast Horizon (Min.)	POC	This work	[19]	[60]
10	264.56	97.90	71.30	-
20	254.14	111.19	98.53	-
30	258.72	119.86	109.33	-
40	260.19	126.00	119.35	-
50	264.17	131.69	127.49	-
60	263.40	136.66	135.43	116.7
70	263.86	139.82	-	-
80	269.37	143.48	-	-
90	268.16	145.36	-	-
100	266.79	148.65	-	-
110	265.10	151.49	-	-
120	265.33	153.52	-	127.6

Table 5: nMAP (W/m²) of POC, this work, and the best results from [56]

Forecast Horizon (Min.)	POC	This work	[56]
10	21.5	9.6	-
20	22.8	11.9	-
30	24.6	13.4	-
40	26.2	14.7	-
50	27.8	15.8	-
60	29.1	16.8	17.4
70	30.1	17.4	-
80	31.6	18.0	-
90	32.6	18.6	-
100	33.4	19.2	-
110	34.1	19.6	-
120	34.9	20.0	20.9

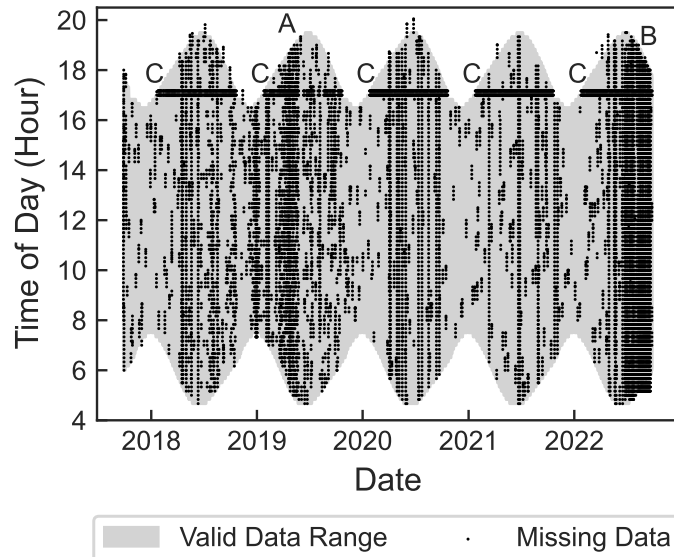


Figure 11: ASI-16 Images missing in the NREL SRRL BMS dataset. A and B were firmware issues noted in the documentation online while C notes a known bug where the camera does not take pictures near 17:00 MST (00:00 GMT)

Integrating the clear sky model and the persistence assumption explicitly into the forecast by changing the representation of future irradiance improves forecasts more than simply providing the clear sky irradiance. These representations simplify model training by isolating the unknown weather effects and not relying on the model to learn already-known long-term dynamics (i.e., de-trending). This work achieves a lower nMAP on the validation period as shown in Table 5 while using a dramatically simpler model.

Figure 11 shows missing data from the ASI-16 sky camera from outages or known firmware issues. Sky camera images are missing after about 17:00 MST in much of the dataset due to a firmware bug. The missing data may contribute to poor model performance, and may cause significant biases in model performance. Our approach was to only use segments of data without missing data-points. Other works using the NREL SRRL BMS such as [56, 19, 60] also selected only complete sequences. Future work could focus on devising more robust models that account for missing data from the sky camera.

Figure 12 shows model prediction MAE boxplots for three distinct sky cover conditions at the time of forecast. The values were computed using the validation data. "Clear" indicates CDOC Total Cloud Cover < 20%, "Partially Cloudy" indicates 20% < CDOC Total Cloud Cover < 80% and "Overcast" indicates CDOC Total Cloud Cover > 80%. Intuitively, clear conditions are more easily predictable as they follow the persistence of cloudiness assumption. The MAE values for over half of the clear sky condition forecasts were small. However, the model may not anticipate changes in sky conditions and the accompanying changes in clear sky index. This is shown by the large volume of high error

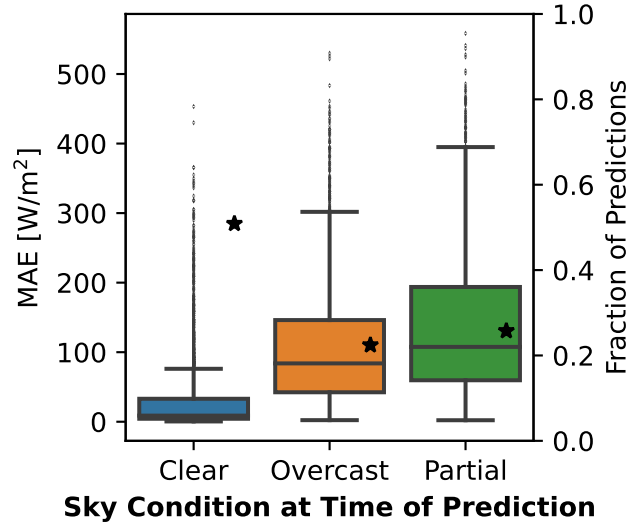


Figure 12: MAE of validation forecasts categorized by three distinct cloud cover conditions: Clear indicates CDOC Total Cloud Cover < 20%, Partially Cloudy indicates 20% < CDOC Total Cloud Cover < 80% and Overcast indicates CDOC Total Cloud Cover < 80%. In addition, the star marker for each cloud cover condition indicates the fraction of predictions within each category.

outliers in the clear sky category. Not unexpectedly, prediction accuracy drops for partially covered and overcast skies. We explain this by considering the naturally higher likelihood of a change in conditions over the forecast horizon from the time of prediction.

6 Conclusions

We developed a data-parsimonious machine learning model for near-term forecasting of solar irradiance. The model relies on a novel CNN-LSTM architecture that includes a noise signal input to account for random/unmeasured variables that influence irradiance.

A training process was proposed, that included probing data representation/feature engineering and feature selection using a sequence of training-validation data sets selected from a publicly available database. The focus was on predictions up to two hours ahead at ten minute intervals, but we expect that other prediction frequencies and near-term horizons can be easily accommodated.

Our findings indicate that predicting the deviation of irradiance from a long-term baseline (e.g., the POC prediction) benefits from a de-trending effect and is thus more accurate than predicting the irradiance itself. We also found that including the noise model (even after eliminating a substantial number of features based on feature importance studies) leads to consistently higher prediction accuracy.

The validation data indicate that the proposed model outperforms other similar results available in the recent literature while requiring orders of magnitude less data as inputs.

Data Availability

The data used for this study were provided by [53]. Code used for data aggregation, modeling, and analysis is available at <https://github.com/joshuaeh/TabularSolarForecast>.

Declaration of Competing Interest

The authors declare that they have no conflict of interest.

Funding Source

Financial support of this work was provided by the Robert A. Welch Foundation (F-1464), the Center for a Solar Powered Future (SPF2050)—an Industry-University Cooperative Research Center (IUCRC) funded by the National Science Foundation (EEC-2052814).

Acknowledgements

The authors would like to thank Drs. Herie Soto, Dhruv Aurora, Hadi Jamali-Rad, Pierre Carrette and Ojas Shreikar for their feedback while working on this research.

CRedit Authorship Contribution Statement

Joshua Hammond: Conceptualization, Methodology, Software, Validation, Formal Analysis, Data Curation, Writing - Original Draft, Visualization. **Ricardo Lara:** Methodology, Software, Validation, Writing - Review & Editing. **Brian Korgel:** Conceptualization, Resources, Writing - Review & Editing, Supervision, Funding Acquisition. **Michael Baldea:** Conceptualization, Methodology, Formal analysis, Writing - Review & Editing, Supervision.

A All Features Studied

The features used in this study are organized by source, with units shown in brackets when applicable:⁵

BMS Meteorological Station Features:

- 315nm Photometer [nA]
- 400nm Photometer [uA]
- 500nm Photometer [uA]
- 675nm Photometer [uA]
- 870nm Photometer [uA]
- 940nm Photometer [uA]
- 1020nm Photometer [uA]
- Snow Depth [cm]
- Precipitation [mm]
- Precipitation (Accumulated) [mm]
- Station Pressure [mBar]
- Tower Dry Bulb Temperature [deg C]
- Tower Relative Humidity [%]
- Snow Depth Quality [%]
- Station Dry Bulb Temp [deg C]
- Station Relative Humidity [%]
- Vertical Wind Shear [1/s]
- Average Wind Speed at 22ft [m/s]
- Average Wind Direction at 22ft [deg from N]
- Peak Wind Speed at 22ft [m/s]
- Albedo (CM3)
- Albedo (LI-200)
- Albedo Quantum (LI-190)
- Broadband Turbidity
- Sea-Level Pressure (Est) [mBar]
- Tower Dew Point Temp [deg C]
- Tower Wet Bulb Temp [deg C]
- Tower Wind Chill Temp [deg C]

⁵More information on the NREL SRRL BMS measurements is available at <https://midcdmz.nrel.gov/apps/html.pl?site=BMS;page=instruments>

- Airmass
- GHI [W/m^2]
- DNI [W/m^2]
- DHI [W/m^2]

Sky Camera Features:

- Blue-Red/Blue-Green Total Cloud Cover [%]
- Cloud Detection and Opacity Correction Total Cloud Cover [%]
- Cloud Detection and Opacity Correction Thick Cloud Cover [%]
- Cloud Detection and Opacity Correction Thin Cloud Cover [%]
- Haze Correction Value
- Blue/Red minimum
- Blue/Red median
- Blue/Red maximum
- Apparent Solar Zenith Angle [deg]
- Apparent Solar Azimuth Angle [deg]
- Flag: Sun not visible
- Flag: Sun on clear sky
- Flag: Parts of sun covered
- Flag: Sun behind clouds, bright dot visible
- Flag: Sun outside view
- Flag: No evaluation

Clear Sky Model Features:

- Clear Sky GHI [W/m^2]
- Clear Sky DNI [W/m^2]
- Clear Sky DHI [W/m^2]
- Solar Eclipse Shading
- Zenith Angle [deg]
- Solar Elevation Angle [deg]
- Solar Azimuth Angle [deg]

Engineered Features:

- Time from sunrise [Days]
- Time to solar noon [Days]
- Time to sunset [Days]
- Cosine time from sunrise [Days]
- Sine time from sunrise [Days]
- Cosine time to solar noon [Days]
- Sine time to solar noon [Days]
- Cosine time to sunset [Days]
- Sine time to sunset [Days]
- Flag: Day
- Flag: Before solar noon
- Cosine zenith angle
- Cosine normal irradiance
- Wind North-South Speed [m/s]
- Wind East-West Speed [m/s]
- Sun North-South Position
- Sun East-West Position
- Time of Day [Days]
- Time of Year [Years]
- Sine Time of Year [Years]

- Cosine Time of Year [Years]
- Sine Time of Day [Days]
- Cosine Time of Year [Days]
- Clear Sky Index GHI
- Clear Sky Index DNI
- Clear Sky Index DHI
- GHI_{t-1} [W/m^2]
- DNI_{t-1} [W/m^2]
- DHI_{t-1} [W/m^2]
- GHI_{t-2} [W/m^2]
- DNI_{t-2} [W/m^2]
- DHI_{t-2} [W/m^2]
- GHI_{t-3} [W/m^2]
- DNI_{t-3} [W/m^2]
- DHI_{t-3} [W/m^2]
- GHI_{t-4} [W/m^2]
- DNI_{t-4} [W/m^2]
- DHI_{t-4} [W/m^2]
- GHI_{t-5} [W/m^2]
- DNI_{t-5} [W/m^2]
- DHI_{t-5} [W/m^2]
- GHI_{t-6} [W/m^2]
- DNI_{t-6} [W/m^2]
- DHI_{t-6} [W/m^2]
- GHI_{t-7} [W/m^2]
- DNI_{t-7} [W/m^2]
- DHI_{t-7} [W/m^2]
- GHI_{t-8} [W/m^2]
- DNI_{t-8} [W/m^2]
- DHI_{t-8} [W/m^2]
- GHI_{t-9} [W/m^2]
- DNI_{t-9} [W/m^2]
- DHI_{t-9} [W/m^2]
- Clear Sky Deviation GHI_t [W/m^2]
- Clear Sky Deviation DNI_t [W/m^2]
- Clear Sky Deviation DHI_t [W/m^2]
- Mean Clear Sky Deviation $GHI_{t-10:t}$ [W/m^2]
- Mean Clear Sky Deviation $DNI_{t-10:t}$ [W/m^2]
- Mean Clear Sky Deviation $DHI_{t-10:t}$ [W/m^2]
- Median Clear Sky Deviation $GHI_{t-10:t}$ [W/m^2]
- Median Clear Sky Deviation $DNI_{t-10:t}$ [W/m^2]
- Median Clear Sky Deviation $DHI_{t-10:t}$ [W/m^2]
- Clear Sky Index Standard Deviation $GHI_{t-10:t}$ [W/m^2]
- Clear Sky Index Standard Deviation $DNI_{t-10:t}$ [W/m^2]
- Clear Sky Index Standard Deviation $DHI_{t-10:t}$ [W/m^2]
- Mean Clear Sky Deviation $GHI_{t-60:t}$ [W/m^2]
- Mean Clear Sky Deviation $DNI_{t-60:t}$ [W/m^2]
- Mean Clear Sky Deviation $DHI_{t-60:t}$ [W/m^2]
- Median Clear Sky Deviation $GHI_{t-60:t}$ [W/m^2]
- Median Clear Sky Deviation $DNI_{t-60:t}$ [W/m^2]
- Median Clear Sky Deviation $DHI_{t-60:t}$ [W/m^2]
- Clear Sky Index Standard Deviation $GHI_{t-60:t}$ [W/m^2]
- Clear Sky Index Standard Deviation $DNI_{t-60:t}$ [W/m^2]
- Clear Sky Index Standard Deviation $DHI_{t-60:t}$ [W/m^2]

References

- [1] A. K. Magnan, H. O. Pörtner, V. K. Duvat, M. Garschagen, V. A. Guinder, Z. Zommers, O. Hoegh-Guldberg, J. P. Gattuso, Estimating the global risk of anthropogenic climate change, *Nature Climate Change* 11 (10) (2021) 879–885. doi:10.1038/s41558-021-01156-w.
- [2] A. Guterres, The Sustainable Development Goals Report 2022, United Nations publication issued by the Department of Economic and Social Affairs (2022) 64.
- [3] J. Biden, [Executive order 12008: Tackling the climate crisis at home and abroad](#), Federal Register (2021) 7619–7633.
URL <https://www.federalregister.gov/d/2021-02177>
- [4] P. Denholm, P. Brown, W. Cole, T. Mai, B. Sergi, M. Brown, P. Jadun, J. Ho, J. Mayernik, M. Colin, R. Sreenath, [Examining Supply-Side Options to Achieve 100 % Clean Electricity by 2035](#), Tech. rep., National Renewable Energy Laboratory, Golden, Co (2022).
URL <https://www.nrel.gov/docs/fy22osti/81644.pdf>
- [5] [Electric Power Monthly with Data for October 2022](#) (2022).
URL http://www.eia.gov/electricity/monthly/epm_table_grapher.cfm?t=epmt_5_06_a
- [6] O. Gandhi, W. Zhang, D. S. Kumar, C. D. Rodríguez-Gallegos, G. M. Yagli, D. Yang, T. Reindl, D. Srinivasan, The value of solar forecasts and the cost of their errors: A review (jan 2024). doi:10.1016/j.rser.2023.113915.
- [7] X. Chen, Y. Du, E. Lim, H. Wen, K. Yan, J. Kirtley, [Power ramp-rates of utility-scale PV systems under passing clouds: Module-level emulation with cloud shadow modeling](#), *Applied Energy* 268 (April) (2020) 114980. doi:10.1016/j.apenergy.2020.114980.
URL <https://doi.org/10.1016/j.apenergy.2020.114980>
- [8] E. Spyrou, V. Krishnan, Q. Xu, B. F. Hobbs, What Is the Value of Alternative Methods for Estimating Ramping Needs?, *IEEE Green Technologies Conference 2020-April* (2020) 159–164. doi:10.1109/GreenTech46478.2020.9289786.
- [9] K. Lappalainen, J. Kleissl, Analysis of the cloud enhancement phenomenon and its effects on photovoltaic generators based on cloud speed sensor measurements, *Journal of Renewable and Sustainable Energy* 12 (4). doi:10.1063/5.0007550.
- [10] X. Chen, Y. Du, E. Lim, L. Fang, K. Yan, Towards the applicability of solar nowcasting: A practice on predictive pv power ramp-rate control, *Renewable Energy* 195 (2022) 147–166. doi:10.1016/j.renene.2022.05.166.
- [11] S. C. Rowe, I. Hischer, A. W. Palumbo, B. A. Chubukov, M. A. Wallace, R. Viger, A. Lewandowski, D. E. Clough, A. W. Weimer, [Nowcasting, predictive control, and feedback control for temperature regulation in a novel hybrid solar-electric reactor for continuous solar-thermal chemical processing](#), *Solar Energy* 174 (July) (2018) 474–488. doi:10.1016/j.solener.2018.09.005.
URL <https://doi.org/10.1016/j.solener.2018.09.005>
- [12] V. Bone, J. Pidgeon, M. Kearney, A. Veeraragavan, [Intra-hour direct normal irradiance forecasting through adaptive clear-sky modelling and cloud tracking](#), *Solar Energy* 159 (October 2017) (2018) 852–867. doi:10.1016/j.solener.2017.10.037.
URL <https://doi.org/10.1016/j.solener.2017.10.037>
- [13] B. Cheng, M. D. Collins, Y. Zhu, T. Liu, T. S. Huang, H. Adam, L. C. Chen, Panoptic-deeplab: A simple, strong, and fast baseline for bottom-up panoptic segmentation, *Proceedings of the IEEE Computer Society Conference on Computer Vision and Pattern Recognition* (2020) 12472–12482 doi:10.1109/CVPR42600.2020.01249.
- [14] B. Li, C. Feng, J. Zhang, Multi-timescale simulation of non-spinning reserve in wholesale electricity markets, *IEEE Green Technologies Conference 2021-April* (2021) 520–527. doi:10.1109/GreenTech48523.2021.00087.
- [15] Q. Li, Q. He, Hourly solar irradiance prediction based on enhanced incremental extreme learning machine, *International Conference on Optoelectronic Information and Functional Materials (OIFM 2022)* 1225519 (2022) 108. doi:10.1117/12.2639376.
- [16] [ERCOT Nodal Protocols \(3.13 Renewable Production Potential Forecasts\)](#) (2022).
URL <https://www.ercot.com/mktrules/nprotocols/current>
- [17] Q. Paletta, G. Arbod, J. Lasenby, [Omnivision forecasting: combining satellite observations with sky images for improved intra-hour solar energy predictions](#) (2022). arXiv:2206.03207.
URL <http://arxiv.org/abs/2206.03207>

- [18] C. Feng, J. Zhang, [Solarnet: A sky image-based deep convolutional neural network for intra-hour solar forecasting](#), *Solar Energy* 204 (2020) 71–78. doi:10.1016/j.solener.2020.03.083. URL <https://doi.org/10.1016/j.solener.2020.03.083>
- [19] C. Feng, J. Zhang, W. Zhang, B. M. Hodge, [Convolutional neural networks for intra-hour solar forecasting based on sky image sequences](#), *Applied Energy* 310 (2022) 118438. doi:10.1016/j.apenergy.2021.118438. URL <https://doi.org/10.1016/j.apenergy.2021.118438>
- [20] V. Le Guen, N. Thome, [Disentangling physical dynamics from unknown factors for unsupervised video prediction](#), *CVPR* (2020) 11471–11481. arXiv:2003.01460, doi:10.1109/CVPR42600.2020.01149. URL <http://arxiv.org/abs/2003.01460>
- [21] A. Dobos, [PVWatts Version 5 Manual - Technical Report NREL/TP-6A20-62641](#), National Renewable Energy Laboratory (NREL) (September) (2014) 20. URL <https://www.nrel.gov/docs/fy14osti/62641.pdf>
- [22] Y. Sun, G. Szűcs, A. R. Brandt, [Solar pv output prediction from video streams using convolutional neural networks](#), *Energy & Environmental Science* 11 (7) (2018) 1811–1818.
- [23] Y. Sun, V. Venugopal, A. R. Brandt, [Short-term solar power forecast with deep learning: Exploring optimal input and output configuration](#), *Solar Energy* 188 (2019) 730–741. doi:10.1016/j.solener.2019.06.041.
- [24] L. Clauzel, S. Anquetin, C. Lavaysse, G. Tremoy, D. Raynaud, [West african operational daily solar forecast errors and their link with meteorological conditions](#), *Renewable Energy* 224 (2024) 120101. doi:10.1016/j.renene.2024.120101.
- [25] P. E. Bett, H. E. Thornton, [The climatological relationships between wind and solar energy supply in britain](#), *Renewable Energy* 87 (2016) 96–110. doi:10.1016/j.renene.2015.10.006.
- [26] P. Ineichen, [A broadband simplified version of the solis clear sky model](#), *Solar Energy* 82 (8) (2008) 758–762. doi:https://doi.org/10.1016/j.solener.2008.02.009. URL <https://www.sciencedirect.com/science/article/pii/S0038092X08000406>
- [27] J. S. Stein, C. W. Hansen, M. J. Reno, [Global horizontal irradiance clear sky models: implementation and analysis.](#), Tech. rep., Sandia National Laboratories (SNL), Albuquerque, NM, and Livermore, CA (2012).
- [28] M. M. Mikofski, C. W. Hansen, W. F. Holmgren, G. M. Kimball, [Use of measured aerosol optical depth and precipitable water to model clear sky irradiance](#), in: 2017 IEEE 44th Photovoltaic Specialist Conference (PVSC), IEEE, 2017, pp. 110–116.
- [29] R. J. Hyndman, E. Wang, N. Laptev, [Large-scale unusual time series detection](#), in: 2015 IEEE international conference on data mining workshop (ICDMW), IEEE, 2015, pp. 1616–1619.
- [30] R. J. Hyndman, G. Athanasopoulos, [Forecasting: principles and practice](#), 3rd Edition, OTexts, 2021. URL <http://otexts.com/fpp3>
- [31] D. Yang, X. Xia, M. J. Mayer, [A tutorial review of the solar power curve: Regressions, model chains, and their hybridization and probabilistic extensions](#) (2024). doi:10.1007/s00376-024-3229-4.
- [32] H. Wen, Y. Du, X. Chen, E. G. Lim, H. Wen, K. Yan, [A regional solar forecasting approach using generative adversarial networks with solar irradiance maps](#), *Renewable Energy* 216. doi:10.1016/j.renene.2023.119043.
- [33] X. Huang, Q. Li, Y. Tai, Z. Chen, J. Zhang, J. Shi, B. Gao, W. Liu, [Hybrid deep neural model for hourly solar irradiance forecasting](#), *Renewable Energy* 171 (2021) 1041–1060. doi:10.1016/j.renene.2021.02.161.
- [34] G. S. Martins, M. Giesbrecht, [Hybrid approaches based on singular spectrum analysis and k- nearest neighbors for clearness index forecasting](#), *Renewable Energy* 219. doi:10.1016/j.renene.2023.119434.
- [35] F. Chollet, [Deep learning with Python](#), second edition Edition, Manning Publication, 2021. URL <https://www.manning.com/books/deep-learning-with-python-second-edition>
- [36] Z. Peng, D. Yu, D. Huang, J. Heiser, S. Yoo, P. Kalb, [3D cloud detection and tracking system for solar forecast using multiple sky imagers](#), *Solar Energy* 118 (2015) 496–519. doi:10.1016/j.solener.2015.05.037. URL <http://dx.doi.org/10.1016/j.solener.2015.05.037>
- [37] B. Nouri, P. Kuhn, S. Wilbert, N. Hanrieder, C. Prah, L. Zarzalejo, A. Kazantzidis, P. Blanc, R. Pitz-Paal, [Cloud height and tracking accuracy of three all sky imager systems for individual clouds](#), *Solar Energy* 177 (August 2018) 213–228. doi:10.1016/j.solener.2018.10.079. URL <https://doi.org/10.1016/j.solener.2018.10.079>

- [38] S. Song, Z. Yang, H. H. Goh, Q. Huang, G. Li, [A novel sky image-based solar irradiance nowcasting model with convolutional block attention mechanism](#), *Energy Reports* 8 (2022) 125–132. doi:10.1016/j.egy.2022.02.166.
URL <https://doi.org/10.1016/j.egy.2022.02.166>
- [39] F. Lin, Y. Zhang, J. Wang, Recent advances in intra-hour solar forecasting: A review of ground-based sky image methods, *International Journal of Forecasting* 39 (1) (2023) 244–265.
- [40] N. Elizabeth Michael, M. Mishra, S. Hasan, A. Al-Durra, Short-Term Solar Power Predicting Model Based on Multi-Step CNN Stacked LSTM Technique, *Energies* 15 (6). doi:10.3390/en15062150.
- [41] Q. Paletta, A. Hu, G. Arbod, P. Blanc, J. Lasenby, [Spin: Simplifying polar invariance for neural networks application to vision-based irradiance forecasting](#) (2021). arXiv:2111.14507v3.
URL <https://arxiv.org/abs/2111.14507v3>
- [42] Q. Paletta, G. Arbod, J. Lasenby, Benchmarking of deep learning irradiance forecasting models from sky images—an in-depth analysis, *Solar Energy* 224 (2021) 855–867.
- [43] G. Liu, H. Qin, Q. Shen, H. Lyv, Y. Qu, J. Fu, Y. Liu, J. Zhou, [Probabilistic spatiotemporal solar irradiation forecasting using deep ensembles convolutional shared weight long short-term memory network](#), *Applied Energy* 300 (2021) 117379. doi:https://doi.org/10.1016/j.apenergy.2021.117379.
URL <https://www.sciencedirect.com/science/article/pii/S0306261921007820>
- [44] S. M. J. Jalali, M. Khodayar, S. Ahmadian, M. Shafie-Khah, A. Khosravi, S. M. S. Islam, S. Nahavandi, J. P. Catalao, A new ensemble reinforcement learning strategy for solar irradiance forecasting using deep optimized convolutional neural network models, in: *SEST 2021 - 4th International Conference on Smart Energy Systems and Technologies*, 2021, pp. 1–6. doi:10.1109/SEST50973.2021.9543462.
- [45] J. Liu, H. Zang, T. Ding, L. Cheng, Z. Wei, G. Sun, Harvesting spatiotemporal correlation from sky image sequence to improve ultra-short-term solar irradiance forecasting, *Renewable Energy* 209 (2023) 619–631. doi:10.1016/j.renene.2023.03.122.
- [46] E. Oglari, M. Sakwa, P. Cusa, Enhanced convolutional neural network for solar radiation nowcasting: All-sky camera infrared images embedded with exogeneous parameters, *Renewable Energy* 221. doi:10.1016/j.renene.2023.119735.
- [47] M. S. Ghonima, B. Urquhart, C. W. Chow, J. E. Shields, A. Cazorla, J. Kleissl, A method for cloud detection and opacity classification based on ground based sky imagery, *Atmospheric Measurement Techniques* 5 (11) (2012) 2881–2892. doi:10.5194/amt-5-2881-2012.
- [48] A. Kazantzidis, P. Tzoumanikas, A. F. Bais, S. Fotopoulos, G. Economou, [Cloud detection and classification with the use of whole-sky ground-based images](#), *Atmospheric Research* 113 (2012) 80–88. doi:10.1016/j.atmosres.2012.05.005.
URL <http://dx.doi.org/10.1016/j.atmosres.2012.05.005>
- [49] A. Heinle, A. Macke, A. Srivastav, Automatic cloud classification of whole sky images, *Atmospheric Measurement Techniques* 3 (2010) 557–567. doi:10.5194/amt-3-557-2010.
- [50] S. A. Haider, M. Sajid, H. Sajid, E. Uddin, Y. Ayaz, Deep learning and statistical methods for short- and long-term solar irradiance forecasting for islamabad, *Renewable Energy* 198 (2022) 51–60. doi:10.1016/j.renene.2022.07.136.
- [51] D. Makwana, S. Nag, O. Susladkar, G. Deshmukh, S. C. Teja R, S. Mittal, C. K. Mohan, [ACLNet: an attention and clustering-based cloud segmentation network](#), *Remote Sensing Letters* 13 (9) (2022) 865–875. doi:10.1080/2150704X.2022.2097031.
URL <https://doi.org/10.1080/2150704X.2022.2097031>
- [52] Y. Fabel, B. Nouri, S. Wilbert, N. Blum, D. Schnaus, R. Triebel, L. F. Zarzalejo, E. Ugedo, J. Kowalski, R. Pitz-Paal, [Combining deep learning and physical models: a benchmark study on all-sky imager-based solar nowcasting systems](#), *Solar RRL* doi:10.1002/solr.202300808.
URL <https://onlinelibrary.wiley.com/doi/10.1002/solr.202300808>
- [53] T. Stoffel, A. Andreas, Nrel solar radiation research laboratory (srnl): Baseline measurement system (bms); golden, colorado (data), Tech. rep., National Renewable Energy Lab.(NREL), Golden, CO (United States) (1981). doi:10.5439/1052221.
- [54] EKO, Asi-16 Find Clouds Software, <https://www.eko-instruments.com/media/z2aalysq/asi-16-software-manual-find-clouds.pdf> (2018).
- [55] W. F. Holmgren, C. W. Hansen, M. A. Mikofski, pvlib python: a python package for modeling solar energy systems, *Journal of Open Source Software* 3 (29) (2018) 884. doi:10.21105/joss.00884.

-
- [56] H. Gao, M. Liu, Short-term solar irradiance prediction from sky images with a clear sky model, Proceedings - 2022 IEEE/CVF Winter Conference on Applications of Computer Vision, WACV 2022 (2022) 3074–3082 [doi:10.1109/WACV51458.2022.00313](https://doi.org/10.1109/WACV51458.2022.00313).
- [57] J. B. Rawlings, D. Q. Mayne, M. M. Diehl, S. Barbara, Model predictive control: Theory, computation, and design 2nd edition (2022).
- [58] A. Altmann, L. Tološi, O. Sander, T. Lengauer, Permutation importance: a corrected feature importance measure, Bioinformatics 26 (10) (2010) 1340–1347.
- [59] A. M. Stolwijk, H. Straatman, G. A. Zielhuis, Studying seasonality by using sine and cosine functions in regression analysis, Journal of Epidemiology & Community Health 53 (4) (1999) 235–238. [doi:10.1136/jech.53.4.235](https://doi.org/10.1136/jech.53.4.235).
- [60] A. Al-Lahham, O. Theeb, K. Elalem, T. A. Alshawi, S. A. Alshebeili, Sky imager-based forecast of solar irradiance using machine learning, Electronics (Switzerland) 9 (2020) 1–14. [doi:10.3390/electronics9101700](https://doi.org/10.3390/electronics9101700).